PAPER • OPEN ACCESS

MamoRef: an optical mammography device using whole-field CW diffuse reflectance. Presentation, validation and preliminary clinical results

View the article online for updates and enhancements.

Physics in Medicine & Biology

MamoRef: an optical mammography device using whole-field CW diffuse reflectance. Presentation, validation and preliminary clinical results

Nicolás A Carbone[1,2] ⬤, Demián A Vera[1] ⬤, M Victoria Waks-Serra[1] ⬤, Héctor A García[1] ⬤, Daniela I Iriarte[1], Juan A Pomarico[1], Pamela A Pardini[2], Silvana Puca[2], Nora Fuentes[3], María E Renati[3], Pablo H Capellino[3] and Romina Osses[3]

1   Centro de Investigaciones en Física e Ingeniería del Centro de la Provincia de Buenos Aires (CIFICEN, UNCPBA-CICPBA-CONICET), Argentina
2   Bionirs Arg SA. Tandil, Buenos Aires, Argentina
3   Hospital Privado de la Comunidad. Mar del Plata, Buenos Aires, Argentina

E-mail: ncarbone@exa.unicen.edu.ar

Keywords: optical mammography, near-infrared spectroscopy, breast cancer, biomedical optics

Abstract

Objective. MamoRef is an mammography device that uses near-infrared light, designed to provide clinically relevant information for the screening of diseases of the breast. Using low power continuous wave lasers and a high sensitivity CCD (Charge-coupled device) that captures a diffusely reflected image of the tissue, MamoRef results in a versatile diagnostic tool that aims to fulfill a complementary role in the diagnosis of breast cancer providing information about the relative hemoglobin concentrations as well as oxygen saturation. *Approach.* We present the design and development of an initial prototype of MamoRef. To ensure its effectiveness, we conducted validation tests on both the theoretical basis of the reconstruction algorithm and the hardware design. Furthermore, we initiated a clinical feasibility study involving patients diagnosed with breast disease, thus evaluating the practical application and potential benefits of MamoRef in a real-world setting. *Main results.* Our study demonstrates the effectiveness of the reconstruction algorithm in recovering relative concentration differences among various chromophores, as confirmed by Monte Carlo simulations. These simulations show that the recovered data correlates well with the ground truth, with SSIMs of 0.8 or more. Additionally, the phantom experiments validate the hardware implementation. The initial clinical findings exhibit highly promising outcomes regarding MamoRef's ability to differentiate between lesions. *Significance.* MamoRef aims to be an advancement in the field of breast pathology screening and diagnostics, providing complementary information to standard diagnostic techniques. One of its main advantages is the ability of determining oxy/deoxyhemoglobin concentrations and oxygen saturation; this constitutes valuable complementary information to standard diagnostic techniques. Besides, MamoRef is a portable and relatively inexpensive device, intended to be not only used in specific medical imaging facilities. Finally, its use does not require external compression of the breast. The findings of this study underscore the potential of MamoRef in fulfilling this crucial role.

1. Introduction

In women, breast cancer is the most commonly diagnosed cancer with 24.5% of incidence and the leading cause of cancer death 15.5%. Considering both women and men, breast cancer is the most commonly diagnosed cancer (11.7% of total cases), with 6.9% of total cancer death (Ferlay *et al* 2021, Sung *et al* 2021).

Early diagnosis is the key to reducing the death rate. Approximately 20%–50% of patients first diagnosed with primary breast cancer will eventually develop metastatic disease while at the time of diagnoses, around 6% have already reached that stage of disease (Lu *et al* 2009, Weinstein *et al* 2009).

Despite the progress in the diagnosis and screening of breast cancer using a combination of x-ray mammography, ultrasound, magnetic resonance imaging (MRI) and awareness in methods of self and clinical breast exams, there remain several gaps in the screening and diagnostic processes that hinder proper treatment. If the initial screenings and interpretations by physicians fail to yield conclusive results in the classification of lesions, it becomes imperative to employ supplementary diagnostic measures that can verify the actual malignity of a detected abnormality and its association with breast cancer. These additional tests, such as prompt biopsy or short-interval routine mammography, play a crucial role in establishing an accurate diagnosis and ensuring appropriate clinical management. However, even with these tests along with current expertize, more than half the women who undergo biopsies ultimately have no malignant lesion (Yen *et al* 2003, Van Luijt *et al* 2016, Tabar *et al* 2018, Chiarelli *et al* 2020, Luo *et al* 2022); consequently these procedures add excessive stress and unnecessary healthcare costs.

There have been great efforts toward cancer-related research, especially in cancer diagnosis to further advance treatment potential. Currently, the most effective screening method is x-ray mammography. While this is the case, it has a 22% false positive rate in women under the age of 50 (Herranz and Ruibal *et al* 2012, Busch *et al* 2013, Groen *et al* 2017, Parikh *et al* 2018, Portnow *et al* 2021). Additionally, to the best of our knowledge, this method cannot accurately distinguish between benign and malignant tumors by itself (Homer 1985). Usually, this methodology is utilized in combination with ultrasound mammography, yet even when combining both, the false positive rate remains high (Berg *et al* 2016).

Because of the fact that most current clinical modalities for breast cancer diagnosis rely on the observation of morphological changes in tissue, stronger approaches are needed in order to examine or even determine metabolic changes in a quantitative manner. MRI with contrast and positron emission tomography have this ability, yet the implementation of these type of tools is very complex, invasive, expensive, and require extensive expertize. Thus, access to this technology with specialized operators is very difficult to attain in most cases, specially in poor or under developed countries.

1.1. The NIR contribution

New methods are being investigated to fill the critical gap mentioned above. There is strong potentiality to utilize near infrared light (NIR) as a non-invasive, reliable diagnostic tool in the application of breast diagnosis (Nioka and Chance 2005, Rinneberg *et al* 2005, Busch *et al* 2013, Tromberg *et al* 2016, Zhao *et al* 2017, Vasudevan *et al* 2021).

Biological tissues have distinct characteristics that allow light of wavelengths between 600 nm and 900 nm to penetrate them up to a few centimeters (Jacques 2013). Below this range, called *optical window,* hemoglobin absorbs light significantly and above it water absorption increases rapidly, impeding any useful light detection.

Moreover, physically, biological tissues can be described as turbid media. This means that, unlike x-rays, NIR light interacts with them not only through absorption events, but through multiple scattering events as well.

This kind of media can be optically described by using the scattering coefficient, μ_s, a measure of the probability of a photon encountering a scattering event per unit distance traveled; the absorption coefficient μ_a, a measure of the probability of a photon encountering an absorption event per unit distance traveled; the anisotropy coefficient g that refers to a measure of the directional preference of light scattering; and the index of refraction, n. The anisotropy coefficient and the scattering coefficient are sometimes combined into a single coefficient, known as the reduced scattering coefficient, $\mu'_s = \mu_s(1 - g)$.

These optical parameters are properly accounted for by the radiative transfer theory (RTT), which describes light propagation in a wide variety of random media (Martelli *et al* 2022). Solutions to this problem are usually difficult to find and, whenever found, of little practical use due to their lack of generality. However, in the special case of biological tissue, we can take advantage of the diffusive characteristics (i.e. $\mu'_s \gg \mu_a$) of the studied media to reduce the RTT to a typical diffusion equation (DE), which has a wider variety of solutions and applications (Martelli *et al* 2022). Now, the main disadvantage of this approach is the high scattering of biological tissue, which leads to a rather poor spatial resolution when compared to other, well established techniques (typically, a few centimeters for NIRS versus a few millimeters or hundreds of micrometers for x-ray (Huda and Abrahams 2015) and MRI (Lin and Alessio 2009)). Nevertheless, this drawback is greatly compensated by other advantages, such as the ease of operation, non-invasiveness, portability, low cost and, especially, the fact that NIR light is non-ionizing radiation, which implies this technology can be used on patients without concerns regarding issues such as the cumulative radiation in tissue, which are more commonly associated to more aggressive therapies that require the use of ionizing radiation.

Importantly, the absorption of the different components that make up a typical biological tissue depends on the wavelength of light that travels through it. Because of this, within the optical window the development of methods for image formation becomes viable since, as said, this radiation can penetrate several centimeters into the tissue. This implies the potential to obtain the tissue optical properties through different means compared to common techniques and thus constituting an important complementary method to gather diagnosis

information. Especially, light is diffusely reflected as well as transmitted, allowing for the possibility of designing a device that captures this reflected light (in *reflectance geometry*) without the need of external mechanical compression of the tissue. NIR techniques based on these fundaments have been used by several researchers in lung (Sun *et al* 2013, Hachey *et al* 2017), gastric (Teh *et al* 2008, Belia *et al* 2022), esophagus (Maziak 2007), endometrial (Zhang *et al* 2011), and pancreatic (Kondepati *et al* 2005, Hoogstins *et al* 2018) oncology systems.

Because of the optical properties of the constituent molecules of human tissue, NIR light is able to provide valuable data on cell function and biological processes such as blood flow, hemoglobin concentration, and oxygen saturation (Kim *et al* 2010). In fact, NIR imaging has been used to determine the concentration of oxygen saturation of hemoglobin in healthy and cancerous tissue (Nioka and Chance 2005). Cancer tissue differs from normal tissue in its metabolic activity, and density: malignant lesions tend to be surrounded by neovascularization and oxygen-rich blood that feeds its growth (Biswal *et al* 2011). In addition, when tumors grow rapidly or reach a certain size, their central areas may not receive sufficient oxygen to support further growth. This can lead to the formation of necrotic lesions that are rich in deoxygenated blood, even when neovascularization is present in the peripheral region. Prior studies show unique scattering and/or absorption signatures associated with dysplastic, malignant and benign tissue transformations (Taroni *et al* 2017, Ntziachristos and Chance 2000, Tromberg *et al* 2000).

In this work we introduce MamoRef, an innovative continuous wave, wide-field reflectance device that aims to use NIR to detect, characterize and follow the evolution of neoplastic lesions of the breast.

In order to better understand the hardware design, some aspects of the whole imaging process that were the subject of previous works must be stressed out. Images are normalized to the background intensity to emphasize the difference between homogeneous tissue (the background) and any inhomogeneity that may be present. We tested this through numerical Monte Carlo (MC) simulations (Carbone *et al* 2017) and phantoms that simulate biological tissues (Serra *et al* 2022). We further studied detectability limits and the potential to obtain 3D information of the position and characteristics of the inclusion; results indicated (i) detection of absorption variations is achieved if images are normalized to background intensity and (ii) inclusions are detected in realistic conditions of depth and absorption contrast for breast lesions (Carbone *et al* 2014). Moreover, we proposed a method to normalize reflectance images using only experimental data; results indicated that it is useful to increase the contrast of the absorption channel (Carbone *et al* 2015, 2017).

Additionally, and in order to progress to a clinical-class prototype, another important point to consider is that clinical applications require a flat surface to be imaged by the camera. This is achieved by a transparent interface, against which the breast is pressed by the body weight. We compared the performance of the method when such an interface was present, to the case of the exposed phantom's surface. Several index matching materials were included in the study and a validation using MC simulations was presented (Carbone *et al* 2017).

This manuscript is structured as follows. Section 2 describes MamoRef's principle of working, together with the details on hardware/software design and the photon migration theory implemented to perform the reconstruction of relative chromophore concentration maps. Section 3 introduces the main results obtained by MC simulations and phantom experiments, as well as results from the first clinical measurements on patients having both malignant and benignant lesions. Finally, section 4 introduces the conclusions related to this work, together with future ideas to improve the hardware implementation and the reconstruction algorithm.
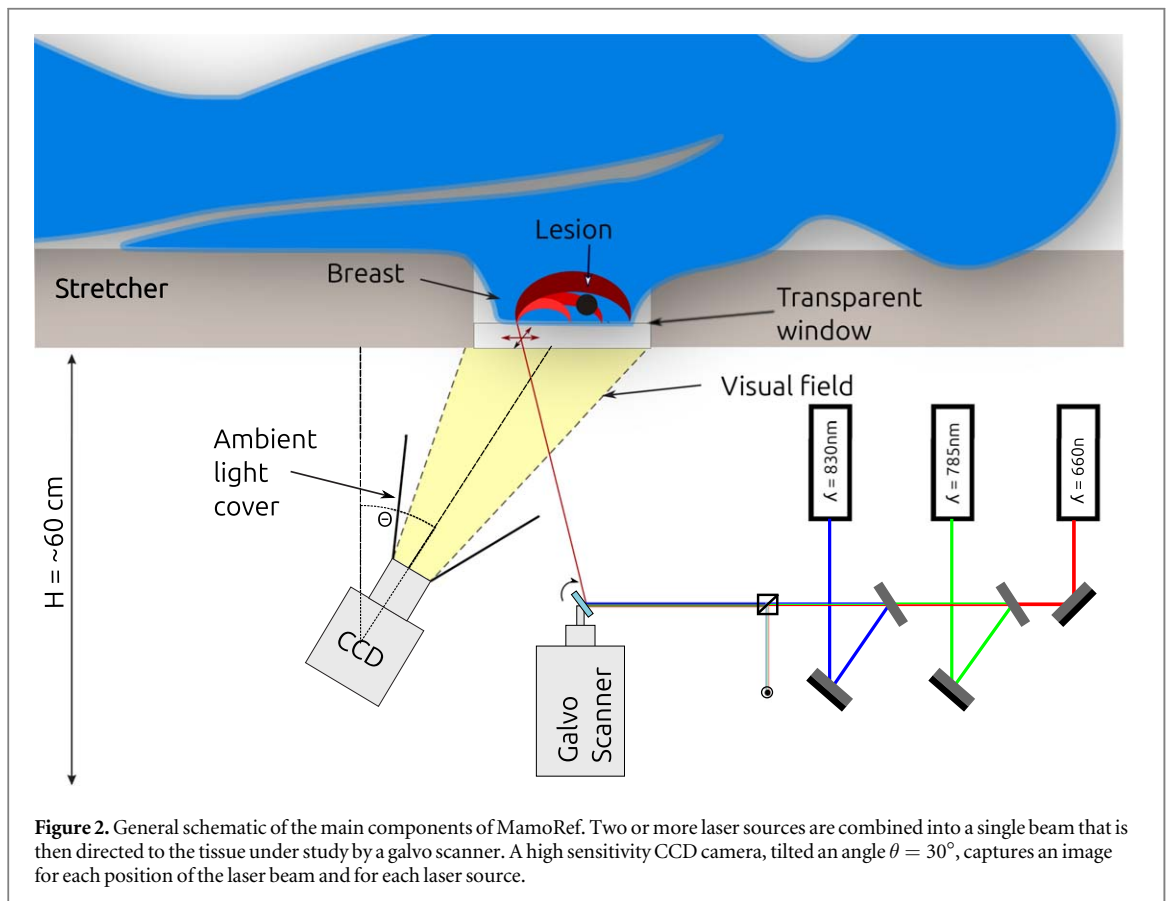
2. Methods

The objective of MamoRef is to find and characterize the metabolic behavior of possible inhomogeneities in the breast tissue, which may be the result of several neoplastic pathologies.

To this end, and due to the fact that the extinction coefficients of tissue's compounds, such as oxygenated hemoglobin (HbO) and deoxygenated hemoglobin (HbR), strongly depend on light's wavelength, it is possible to obtain maps of oxy- and deoxygenated blood using at least two wavelengths (see figure 1 (Suzaki *et al* 2006, Tabulated molar extinction coefficient for hemoglobin in water 2022)); these maps are directly relatable to metabolic function and, as mentioned before, could in principle allow the differentiation of distinct types of inhomogeneities. Thus, the MamoRef approach relies on acquiring, by a CCD camera, diffusely reflected light images of the breast under study, which may contain lesions (bening or malignant) with optical properties, i.e. scattering and absorption coefficients, that differ from those of the healthy background tissue.

2.1. Hardware design
The general design of MamoRef is shown in schematic form in figure 2. It consists of a stretcher with a transparent window under which the measurement system is placed. The patient lies *decubito prono* on the stretcher with the breast being scanned resting on the window. Contrary to x-ray mammography, in which

Figure 1. Relative absorption spectra for HbO (red curve) and HbR (blue curve). The green lines mark the lasers wavelengths used in MamoRef.

Figure 2. General schematic of the main components of MamoRef. Two or more laser sources are combined into a single beam that is then directed to the tissue under study by a galvo scanner. A high sensitivity CCD camera, tilted an angle $\theta = 30°$, captures an image for each position of the laser beam and for each laser source.

artificial compression of the breast is required, here no mechanical compression other than the one produced by the body weight itself is needed.

This arrangement flattens the patient's breasts in a relatively comfortable way; this allows to correctly model the acquisition as a reflectance measurement. Moreover, as we are taking a photograph of the tissue that is under study, flattening its surface allows for a completely in-focus picture with homogenous exposure.

The basic components of the optics measurement system are at least two CW lasers, a high sensitivity CCD camera, and a galvanometric scanner, that allows directing the laser beams towards the area to study. In order to determine the oxy- and deoxyhemoglobin concentration the mentioned lasers must be of different wavelengths

within the optical window and on each side of the isosbestic point of the hemoglobin (∼800 nm), as shown on figure 1. In the current version of MamoRef, a third laser is present with $\lambda = 785$ nm that can be used as a reference signal if needed.

For each position of the laser and for all wavelengths involved, an image of the entire field is taken. These images are then fed into an algorithm that cleans, processes and reconstructs a final image ready for clinical evaluation by trained physicians. It is important to note that the specific dimensions of the 2D grid depend on the chosen region of interest (ROI), a parameter inherently influenced by the size of the breast under examination. Furthermore, the ROI may assume an elliptical shape, and adjustments to the separation between adjacent scan positions can be made as needed. Typically, the comprehensive rectangular grid encompasses dimensions ranging from 6×6 to 10×10 scan positions. Specifically, over the 42 clinical cases studied to the date, the mean number of scan positions is 68 with a standard deviation of 19.

The CCD camera, a Kiralux CS505MU (Thorlabs CS505MU 2023) from Thorlabs, and the galvo scanner (ThorLabs GVS012/M 2D Large Beam (10 mm) Diameter Galvo System (Thorlabs GVS012/M 2023)) used for the results presented in this publication are both off-the-shelf parts.

The Kiralux camera was selected since it is a relatively inexpensive camera with good sensibility in the near infrared portion of the spectrum and includes an open Software Development Kit (SDK). More sensitive cameras are being evaluated for future prototypes of MamoRef. Attached to the camera was a 12 mm focal length, $f/1.4$ maximum aperture, C-Mount lens, also from ThorLabs (Thorlabs mvl12m1 2023). To prevent the lens from capturing the specular reflection of the laser beam on the transparent window, the CCD camera is positioned at an angle $\theta = 30°$ with respect to the center of the viewing area. Additionally, a specially designed conical hood is placed around the lens to minimize the chances of other reflections entering it.

Since precise positioning of the laser beams onto the surface under study is important for the reconstruction of the final image, the used galvo scanner was chosen because of its reliability and easy availability. It must be noted that this galvo scanner surpasses the minimum requirements for both positioning precision and speed necessary for MamoRef. In terms of speed, the galvo scanner's velocity governs the time it takes for the laser beam to move from one position to the next within the scanning grid. This time is significantly low, even in low-speed galvo scanners, compared to the camera exposure time. The precision requirements for the galvo scanner are also relatively lenient. The typical angular separation between two adjacent points is approximately 1°, much greater than the angular resolution of any scientific-grade galvo scanner. Future implementations can consider utilizing alternative galvo scanner models, potentially offering lower precision but also at a lower cost compared to the current one, without compromising MamoRef's performance.

In its current set-up MamoRef uses three CW diode lasers operating at $\lambda_1 = 660$ nm, $\lambda_2 = 785$ nm and $\lambda_3 = 830$ nm (all of them selected from the Coherent Stingray Series (Coherent stingray diode lasers 2023)), such as to match the different absorptions of HbO and HbR. Despite the fact that two of them ($\lambda = 785$ nm and $\lambda = 830$ nm) can operate at powers of up to 15mW, all three were limited down to 5 mW via a simple serial protocol for both, experiments on phantoms and on volunteers. Care was taken such as not to surpass the maximum allowed intensity for human security. Coherent supplies heat sinks specifically designed for use with their lasers, which were utilized without any modifications. The operational temperature of the laser module is continuously monitored and typically maintained below 40 °C. Figure 3 shows the laser assembly. The objective is to generate a single beam combining the three lasers. While they are only used one at a time, having a single beam greatly simplifies the scanning process. In order to achieve this, two short-pass dichroic mirrors are used, one allowing the transmission of the 660 nm beam and reflecting the 785 nm beam; and the other allowing the transmission of both the 660 and 785 nm beams while reflecting the 830 nm beam. First-surface silvered mirrors placed on a tilting mount are used for both, allowing fine calibration of the individual beams and ensuring that the beams fall onto the dichroic mirror at an optimum angle accordingly to their specifications. A 90:10 beam splitter is placed in the common way of all three lasers to sample 10% of the beam power. This makes it possible to keep constant the power of the active laser by means of a feedback circuit. In figure 3(a) a schema of the above mentioned assembly is shown. Figure 3(b) shows a photograph of the laser assembly in the current MamoRef prototype.

The combined laser beams are directed (one at a time) to the galvo scanner mirrors that direct the active beam to the exact corresponding position on the inferior surface of the window pane. The galvo scanner takes two analog signals, a bipolar ± 15 V DC stable power supply, and another one between -10 and $+10$ V to control the position of the mirrors. A customized printed circuit board, based on a PDQ15-Q48-S15-D power supply (Pdq15-q48-s15-d power supply 2023) and a TI-DAC8871 digital to analog converter (DAC) (16-bit single channel 2023), was used to generate the input power and the control signals. This card also incorporates the required USB-to-Serial interface to control the lasers using a STM32F103 microcontroller (Stm32f103 microcontroller 2023).

The whole system is enclosed in a light-tight black box. Figure 4(a) shows a 3D CAD of the location of each component. Each individual component is attached to perforated panels using specially designed and 3D-
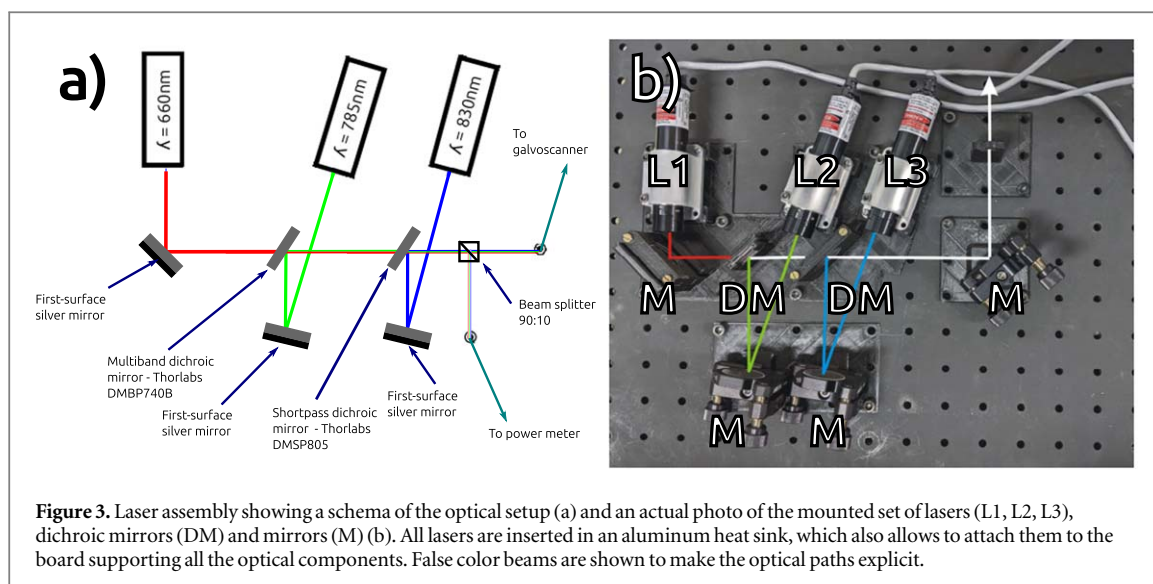
Figure 3. Laser assembly showing a schema of the optical setup (a) and an actual photo of the mounted set of lasers (L1, L2, L3), dichroic mirrors (DM) and mirrors (M) (b). All lasers are inserted in an aluminum heat sink, which also allows to attach them to the board supporting all the optical components. False color beams are shown to make the optical paths explicit.
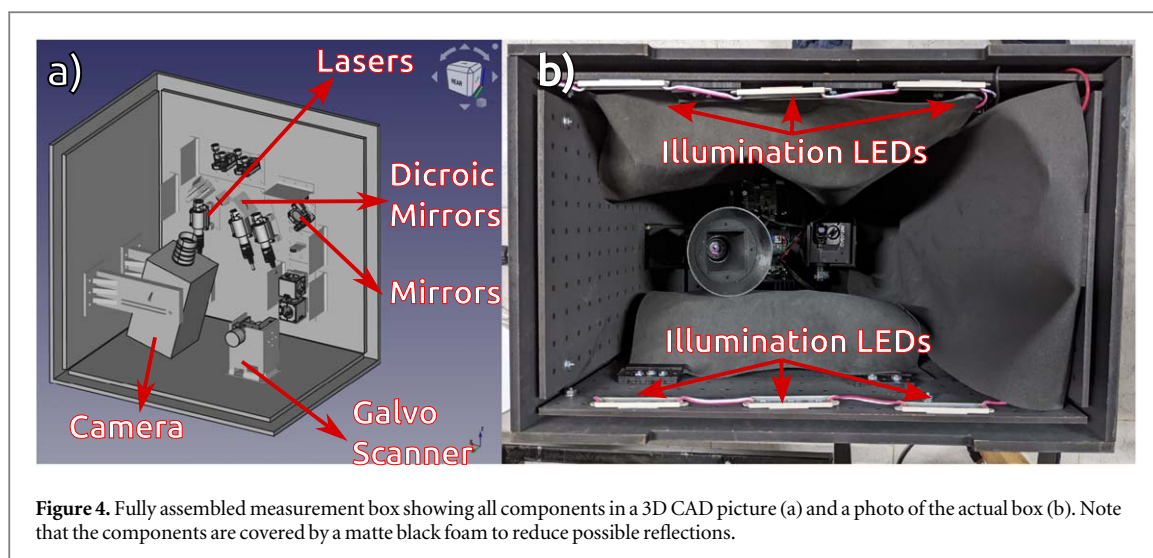

Figure 4. Fully assembled measurement box showing all components in a 3D CAD picture (a) and a photo of the actual box (b). Note that the components are covered by a matte black foam to reduce possible reflections.

printed attachment adapters. One of the lateral faces of the box is used to support the lasers and mirrors; the galvo scanner is fixed to the bottom wall and the camera is fixed to another lateral wall with the lens facing upwards towards the surface to be measured. Figure 4(b) is a photo of the assembled box. Pieces of matte black foam are located to minimize possible unwanted reflections.

The black box is placed under the stretcher and a transparent window, made of PMMA, separates the upper part of the stretcher, where the patient is to lay down, from the measurement box. Figure 5 shows a 3D rendering of the arrangement and a photo of the actual assembly.

2.2. Calibration

An initial calibration is always required after hardware modifications or transport. This calibration serves to construct functions that (i) are able to translate galvo scanner positions, measured as volts applied to each step-motor's driver, to screen-space pixel positions of the laser, and (ii) to correct perspective distortion effects as a result of off-axis position of the camera. Once this calibration is done, does not require medical staff to be performed and should persist between measurements, provided that the device needs not to be translated or modified. Future versions of this device will ensure that the calibration frequency strongly reduces.

2.3. Control software

MamoRef is controlled by a graphical user interface (GUI) programmed in Python and tkinter. It allows the user (medical or technical staff from the associated hospital) easy control of the main configuration parameters of the measurement. While still under development, the GUI has proved to be adequate enough for the first clinical
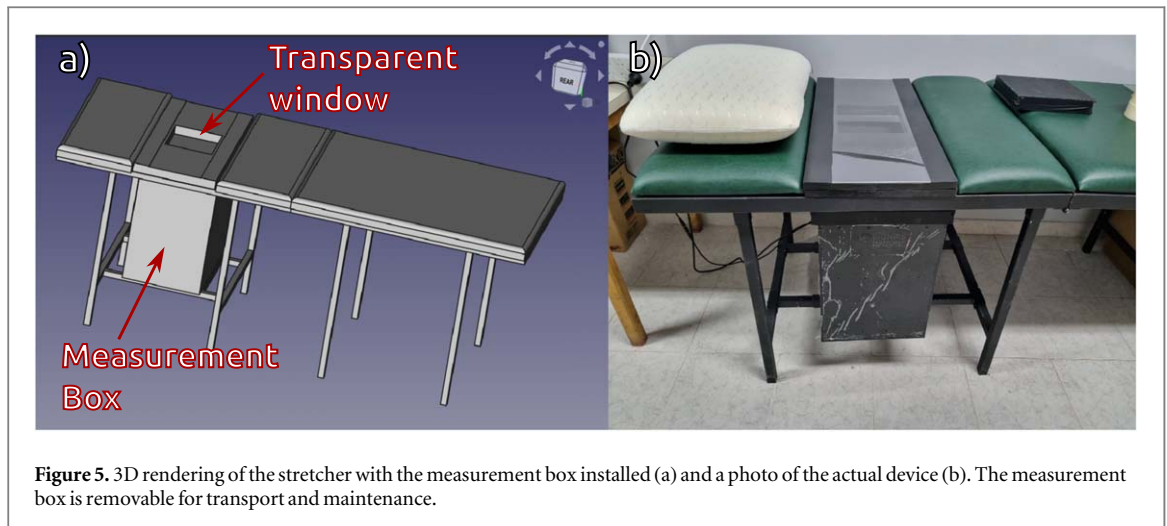
Figure 5. 3D rendering of the stretcher with the measurement box installed (a) and a photo of the actual device (b). The measurement box is removable for transport and maintenance.
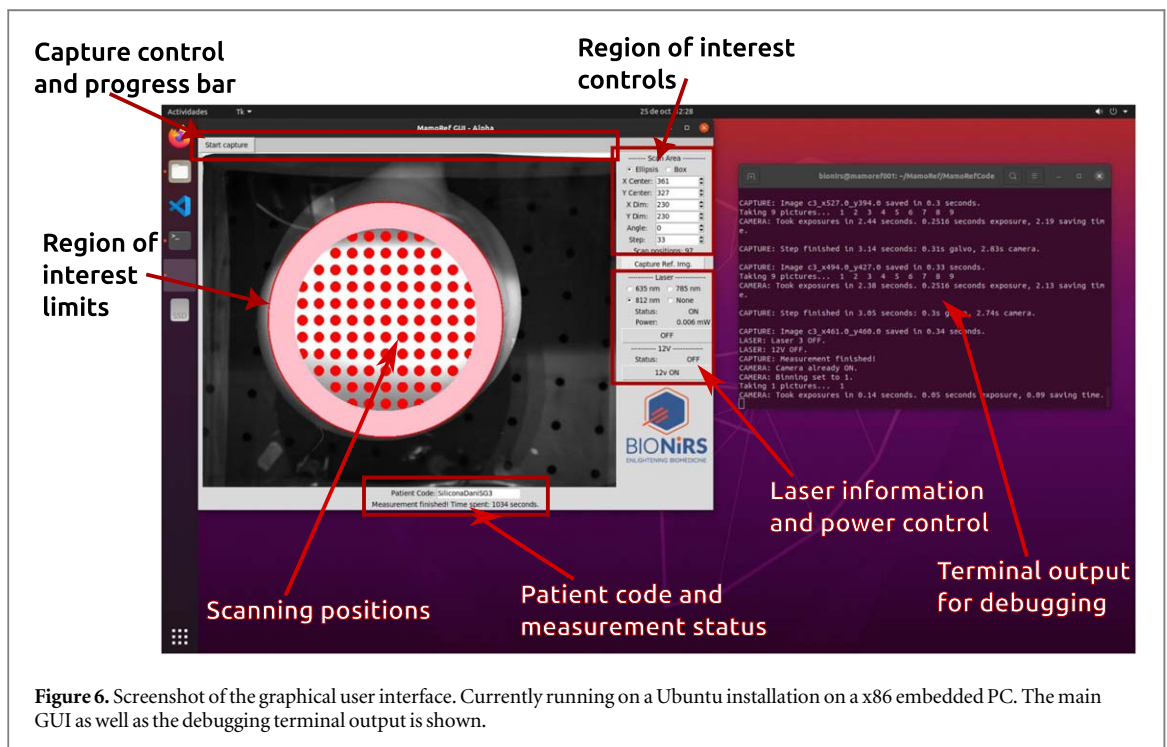

Figure 6. Screenshot of the graphical user interface. Currently running on a Ubuntu installation on a x86 embedded PC. The main GUI as well as the debugging terminal output is shown.

trials. Figure 6 shows a screenshot of the GUI while measuring a test phantom. It has the following functionalities:

- **Selection of the region of interest** (**ROI**): used to select the area to scan. The current version of the GUI allows to select an ellipse or rectangular shaped ROI using numeric controls.

- **Laser control and status visualization**: this area shows the active laser and its current power output. It also allows to shutdown either individual lasers or the 12 V power supply to all the lasers simultaneously. In future versions of the device an emergency stop button to shutdown all the lasers will be added/implemented. While not strictly necessary (all lasers operate at powers $\leqslant$5 mW) it is important for a medical setting.

- **Reference image and scanning positions visualization**: a reference image using red light illumination can be captured in order to help accurately select the ROIs. To this end, six LED stripes are placed inside the box and controlled via software, as shown in figure 4(b). When a ROI is configured, the scanning positions are shown over-imposed to the image. Also, while the measurement is in process, the current laser position is displayed.

- **Capture start and stop button and progress bar**: this button controls the start of the measurement process and can be used to stop it at any time. A progress bar provides visual feedback about the completed percentage of the measurement.

- **Patient code input**: an anonymous patient code is appended to the output files and as a field in a text file that stores the measurement configurations.

- **Measurement status display**: in this area the current stage of the measurement is displayed in text format. Also an estimated remaining time is shown.

At this stage, a terminal is also executed showing debugging outputs. This will be optionally hidden in a future version of the GUI. The output is also logged in an external file that remains between measurements to diagnose possible malfunctions.

Once the measurement is started, a different software runs parallel to the GUI. This software, also written in Python, controls the hardware that performs the actual measurement through the following steps:

(i) Takes a reference image illuminated with an expanded LED-based red light source and a background noise image with all light sources off.

(ii) Performs a quick re-calibration of the galvo scanner analog voltage input to pixel transform function to account for possible small miss-calibrations that could have happened in between measurements.

(iii) For each laser:

   (a) Turns it on.

   (b) For each of the N scans position (usually around 30–60, is user selectable and depends on breast size):

      1. Reads the power output and working temperature to ensure them to be at the proper values.

      2. Moves the galvo scanner to the desired position.

      3. Takes M images with increasing exposures levels. M is configurable, and it is usually between 3 and 5.

   (c) Turns it off.

The scan process takes around 2 s per position, including all exposure times and the dead time required to move to the next point; thus, a typical whole scan for an average size breast with $N = 60$ takes roughly 6 min and should take less than 10 min even for the largest breast sizes.

2.4. Attenuation maps reconstruction algorithm

Considering that two wavelengths are used, the complete set of raw data obtained from MamoRef consists in $2 \times N \times M$ were 2 represents the number of wavelengths used, N is the scanning position and M the number of images taken in that position. To these images another two are added, namely the background and reference images.

As previously stated, the main objective is to obtain a whole-field relative attenuation map for each laser wavelength that must then be further analyzed to extract medical relevant information like HbR and HbO relative concentrations. In order to do this, the raw images are processed using an algorithm that:

1. Cleans the images using a background image that takes into account ambient noise and CCD electronic noise.

2. For each image, determines the position of the laser beam and crops a region around it.

3. The mosaics obtained are averaged in order to blur the inhomogeneities in case that they are present. This image is then used to normalize each one of the mosaics.

4. Each of the cropped images is normalized using the image created in the previous step. This normalization is necessary to homogenize the exposure of the entire explored area and enhance the presence of inhomogeneities.

5. The normalized cropped images are placed back in their original positions, reconstructing a normalized full-field image where the presence of inhomogeneities in the studied tissue can be evaluated.

Currently, this algorithm is implemented in Python and a sample code and data are provided in GitHub (Github public repository of sample code 2023). A typical reconstruction takes around 15 min in a modern Ryzen 7 5800x3D with 32 Gb of RAM for experimental data with 60 scanning positions.

2.5. Using multiple wavelengths to recover HbO and HbR relative concentrations

The data preprocessing steps described in the previous Subsection lead to an attenuation map $A(\lambda, \mathbf{r})$ as a function of the wavelength, λ, and the position, $\mathbf{r}$, which can basically be interpreted as a map of detected light intensity $I(\lambda, \mathbf{r})$ relative to a reference or background signal $I_0(\lambda, \mathbf{r})$. Actually, since measurements are carried out at the surface of the medium, $z = 0$, so we can write instead $A(\lambda, \mathbf{r}) \equiv A(\lambda, \rho)$, with $\rho = \sqrt{x^2 + y^2}$.

This attenuation map is related to the reference absorption $\Delta\mu_a(\lambda)$ that characterizes the medium by the well-known modified Beer–Lambert law (MBLL) (Almajidy *et al* 2020):

$$A(\lambda, \rho) = -\log\left[\frac{I(\lambda, \rho)}{I_0(\lambda, \rho)}\right] = L(\lambda, \rho)\Delta\mu_a(\lambda),\tag{1}$$

where $L(\lambda, \rho)$ is the total mean pathlength of photons in the medium (Hiraoka *et al* 1993, Martelli *et al* 2022). In the particular case of a sufficiently thick homogeneous slab, this quantity takes the form (Contini *et al* 1997):

$$L(\lambda, \rho) = -\frac{1}{8\pi D_0 I_0(\lambda, \rho)}\sum_{m=-\infty}^{\infty}\left(z_{3m}(\rho^2 + z_{3m}^2)^{-1/2} \times \exp\left\{-\left[\frac{\mu_{a0}(\rho^2 + z_{3m}^2)}{D_0}\right]^{1/2}\right\} - \right.$$

$$\left. -z_{4m}(\rho^2 + z_{4m}^2)^{-1/2} \times \exp\left\{-\left[\frac{\mu_{a0}(\rho^2 + z_{4m}^2)}{D_0}\right]^{1/2}\right\}\right),\tag{2}$$

being $D_0 = (3\mu'_{s0})^{-1}$ the diffusion coefficient, μ_{a0} and μ'_{s0} the background optical properties, and z_{3m} and z_{4m} a set of image light sources at both sides of the slab needed to fulfill the boundary conditions (Contini *et al* 1997). Here it must be noted that $L(\lambda, \rho)$ depends on the wavelength not only through the input signal $I_0(\lambda, \rho)$, but also through the background optical properties. However, and as in any fitting routine, these quantities are in general unknown, so their values must be inferred or at least assumed; to this end, we fed the reconstruction algorithm with typical values of the optical properties (Vo-Dinh 2002), which led to setting $L(\lambda, \rho) \approx L(\rho)$.

Next, the relative absorption in biological tissues can be modeled by the presence of HbO and HbR. The conversion between relative absorption and relative chromophore concentrations (symbolized with squared brackets) is given by Kocsis *et al* (2006), Pellicer and Bravo (2011):

$$\Delta\mu_a(\lambda) = \varepsilon_{HbO}(\lambda)\Delta[HbO] + \varepsilon_{HbR}(\lambda)\Delta[HbR],\tag{3}$$

being $\varepsilon_{HbO}(\lambda)$ ($\varepsilon_{HbR}(\lambda)$) the molar extinction coefficient of HbO (HbR) at wavelength λ. Expressions (1) and (3) can be combined in matrix form to give the following equation:

$$\begin{bmatrix} A(\lambda_1, \rho) \\ A(\lambda_2, \rho) \end{bmatrix} = L(\rho)\begin{bmatrix} \varepsilon_{HbO}(\lambda_1) & \varepsilon_{HbR}(\lambda_1) \\ \varepsilon_{HbO}(\lambda_2) & \varepsilon_{HbR}(\lambda_2) \end{bmatrix}\begin{bmatrix} \Delta[HbO] \\ \Delta[HbR] \end{bmatrix}.\tag{4}$$

This matrix equation can be easily solved for each pixel of the image to obtain $\mathbf{\Delta[HbX]} = [\Delta[HbO], \Delta[HbR]]^T$. Please note that two different wavelengths (i.e. $\lambda_1 \neq \lambda_2$) are needed in order to solve equation (4) for the two unknowns $\Delta[HbO]$ and $\Delta[HbR]$.

As an additional step, relative oxygen saturation can be calculated using the following expression:

$$SatO_2 = \frac{HbO}{HbR + HbO}.\tag{5}$$

It is important to note that since we are retrieving relative hemoglobin concentrations, the resulting oxygen saturation will also be relative to the surrounding medium. While this may appear as a limitation, the ability to map the oxygen saturation of the entire breast (or region of interest) is a novel and valuable approach for assessing potential malignancy levels in conjunction with relative hemoglobin concentration and prior knowledge.

3. Results and discussion

After developing the reconstruction algorithm as previously introduced and designing and building a first prototype device, we conducted tests to validate the functionality of both the software and hardware components.

To ensure the accuracy of our assessments, we provided both the software and hardware with known data, such as a chromophore distribution, which could then be compared to the retrieved values. Two well-

established techniques were utilized for this purpose. Firstly, Monte-Carlo simulations were performed to test the reconstruction algorithm. Secondly, phantom experiments were carried out to test both the reconstruction algorithm and the data retrieval capabilities of the MamoRef device.

3.1. Monte Carlo simulations

Monte Carlo simulations are considered a gold-standard as they are able to accurately model the propagation of light in turbid media without major assumptions or simplifications (Prince and Malarvizhi 2007, Shi and Anderson 2010, Carbone *et al* 2017, Vera *et al* 2022). For MamoRef, we performed simulations with different kinds of inclusions using Monte Carlo eXtreme GPU-accelerated photon transport simulator (Monte Carlo extreme 2023). Mimicking the way MamoRef captures real images, in the simulations several source positions were considered to simulate the scanning process and, for each one, a whole-field reflectance image was computed.

To assess the quality of the reconstructions, we compared, by means of the structural similarity index measure (SSIM), the resulting images with a reference ('perfect') image built using the information about geometrical and optical properties of the bulk and inclusions applied in the MC simulations (Brunet *et al* 2011, Dosselmann and Yang 2011).

A slab-like background medium of size $250 \times 250 \times 60$ mm^3 with reduced scattering coefficient $\mu'_s = 1$ mm^{-1} and absorption coefficient $\mu_a = 0.01$ mm^{-1} was simulated. Embedded in it, two spherical inclusions were placed, one emulating a high HbO lesion, located at (175, 125, 10) mm and another simulating a low HbO lesion placed at (75, 125, 10) mm that represent a benign and a malignant tumor respectively. Three simulations were conducted by varying the X positions of inclusions, resulting in separations of 15 mm, 20 mm, and 25 mm in each respective simulation. This approach was employed to evaluate the resolution capabilities of the technique. The inclusions were chosen to simulate the solid masses of two clinical examples showed in the work done by Biswal *et al* (2011): one benign fibroadenoma and one invasive carcinoma. Both inclusions were spherical-shaped with a diameter of 10 mm.

The adenocarcinoma (inclusion 1, left) had an absorption coefficient of 0.0243 mm^{-1} and 0.0183 mm^{-1} for 660 nm and 830 nm, respectively, corresponding to HbO and HbR concentrations of 25.2 μM and 16.8 μM respectively. The fibroadenoma (inclusion 2, right) had an absorption coefficient of 0.0179 mm^{-1} and 0.019 mm^{-1} for 660 nm and 830 nm, corresponding to HbO and HbR concentrations of 34.8 μM and 7.14 μM, respectively. As a result, the corresponding oxygen saturation values are 60% for inclusion 1% and 83% for inclusion 2.

In addition to the aforementioned simulations, we conducted an assessment of potential impacts arising from the presence of a chest wall beneath the breast tissue. To investigate this, two distinct simulations were performed, maintaining identical inclusions as in the preceding scenario but with a separation distance of 100 mm (x_1=75 mm, x_2=175 mm) along the x-axis. In one simulation, we assumed a homogeneous medium without a chest wall, while in the other one, we introduced a chest wall with optical properties characterized by $\mu'_s = 0.9$ mm^{-1} and $\mu_a = 0.02$ mm^{-1} (Zhang *et al* 2021), positioned at a depth of 20 mm.

The source is displaced in a 6×6 grid; each point of the grid is spaced 30 mm from the next one in both x and y directions, covering the whole entry face of the bulk. For each position of the source 5×10^9 photons were launched. Each simulation took around 14 h running on an PC equipped with a Nvidia Titan Xp, Ryzen 5700X CPU and 64 GB of RAM. Figure 7 shows the results of applying the HbO and HbR reconstruction algorithm to the MC simulation. They are available in the GitHub repository (Github public repository of sample code 2023). Figure 7 shows the reconstructions of HbO, HbR and O$_2$ saturation maps for the situation of the emulated adenocarcinoma (left inclusion) and fibroadenoma (right inclusion) separated by 15 mm (first column), 20 mm (second column) and 25 mm (third column). In the first case, the two inhomogeneities cannot be resolved (first and second rows) but the O$_2$ saturation map (third row) clearly shows the location of the inclusion for which this magnitude is greater than the surrounding medium. When the separation between inclusions is 20 mm or 25 mm they are resolved and the corresponding HbO and HbR concentrations are correctly retrieved in terms of relative values. Moreover, the oxygen saturation values retrieved at the peaks of the HbX concentration profiles (fourth row) are in excellent agreement with the ground truth values (below 3% for both types of inclusions).

Regarding the assessment of the influence of the chest wall, figure 8 shows the comparison of the retrievals of concentration maps of HbO and HbR for a homogeneous healthy tissue (left column) and in the presence of the chest wall (right column) that starts at a depth of 20 mm. As can be seen in the last row, the profiles of HbX concentrations are in excellent agreement with each other. Please note that the baseline value may differ from one map to another, but the relative concentration changes in the region of the inhomogeneities are exactly the same. Table 1 shows the comparison between the retrieved positions and sizes of the inclusions compared to their real ground truths. We see that the recovered positions are in very good agreement with the nominal ones. The size, however, is overestimated, which is the direct result of the scattering nature of the propagation of the
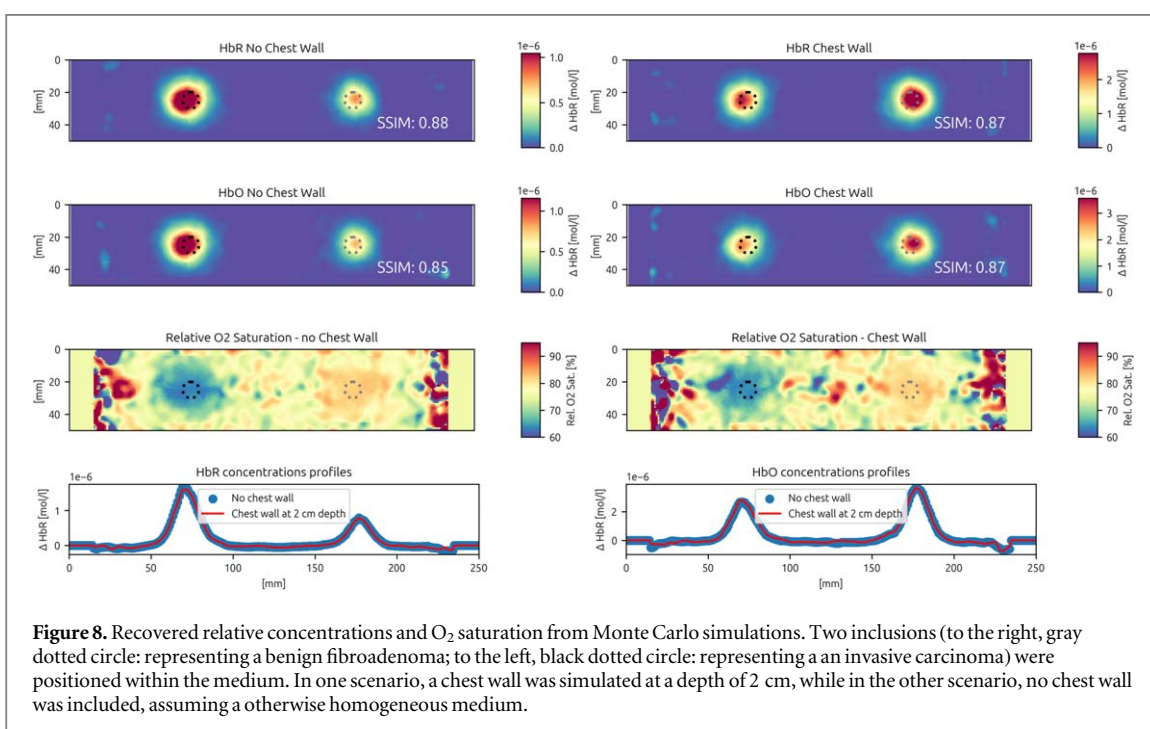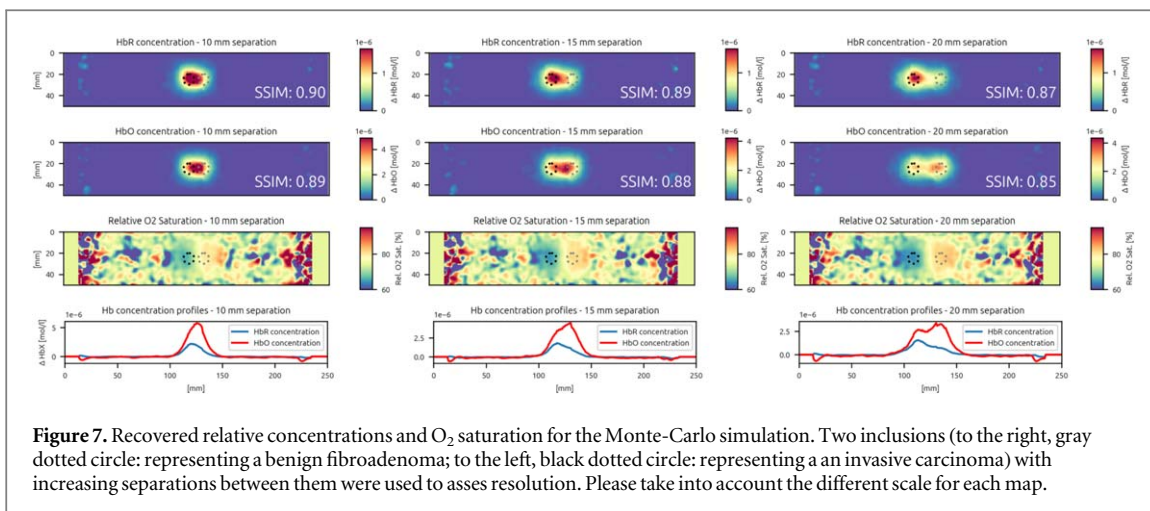
Figure 7. Recovered relative concentrations and O$_2$ saturation for the Monte-Carlo simulation. Two inclusions (to the right, gray dotted circle: representing a benign fibroadenoma; to the left, black dotted circle: representing a an invasive carcinoma) with increasing separations between them were used to asses resolution. Please take into account the different scale for each map.

Figure 8. Recovered relative concentrations and O$_2$ saturation from Monte Carlo simulations. Two inclusions (to the right, gray dotted circle: representing a benign fibroadenoma; to the left, black dotted circle: representing a an invasive carcinoma) were positioned within the medium. In one scenario, a chest wall was simulated at a depth of 2 cm, while in the other scenario, no chest wall was included, assuming a otherwise homogeneous medium.

Table 1. Recovered positions and sizes of the inclusions shown in figure 8 compared with their ground truth.

		Inclusion 1	Inclusion 2
Size [mm]	Ground truth	10	10
	Recovered FWHM	14	13
x position [mm]	Ground truth	75	175
	Recovered	70	177
y position [mm]	Ground truth	125	125
	Recovered	125	125

light in the medium. In all cases, the SSIM is >0.8, indicating a strong similarity between the reconstructed image and the MC ground truth. When interpreting this result, it is essential to consider that the scattering of light within the medium may limit achieving very high SSIM values, even if the reconstruction were flawless. The difference in concentration with respect to the background is within the expected values for the input data
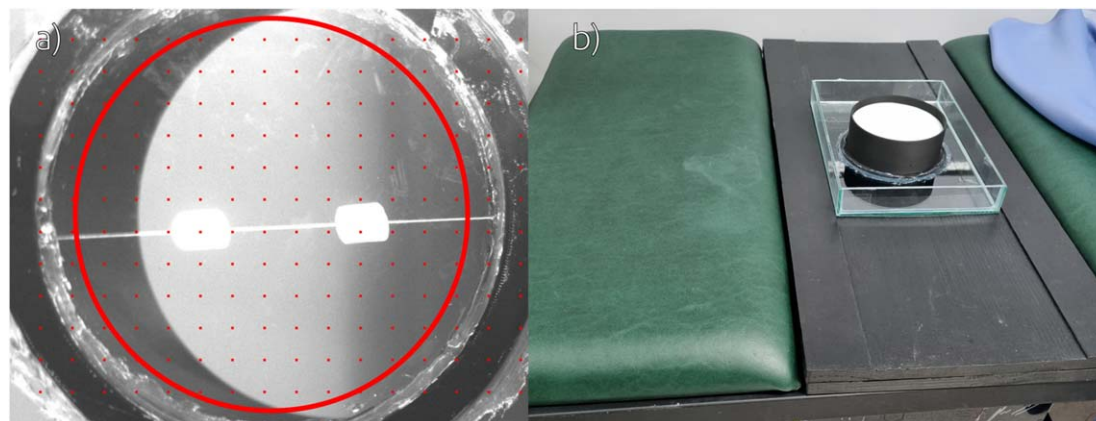
Figure 9. Image, as seen from the MamoRef GUI, of the inclusions previous to filling the bucket with the liquid phantom (a) and a photo of the phantom ready to be measured (b). The inclusion to the left has a higher concentration of Epson ink than the surrounding medium while the one to the right has a higher concentration of ADS ink.

leading to an overall performance of the algorithm similar to others previously reported in the literature (Mozumder *et al* 2022).

3.2. Phantom experiments

While MC simulations are very useful to test the software, they are not performed using the real device and it is very difficult to model all the possible sources of error or noise present in an experimental situation. For these reasons, phantom experiments must be carried out in order to test the experimental paradigm together with the reconstruction algorithm.

In our context, a phantom refers to an object or material, not necessarily anthropomorphic, that is designed to simulate the optical properties of biological tissue. In this case, the phantoms are designed as to emulate the absorption and scattering coefficients of both, healthy and diseased breast tissue.
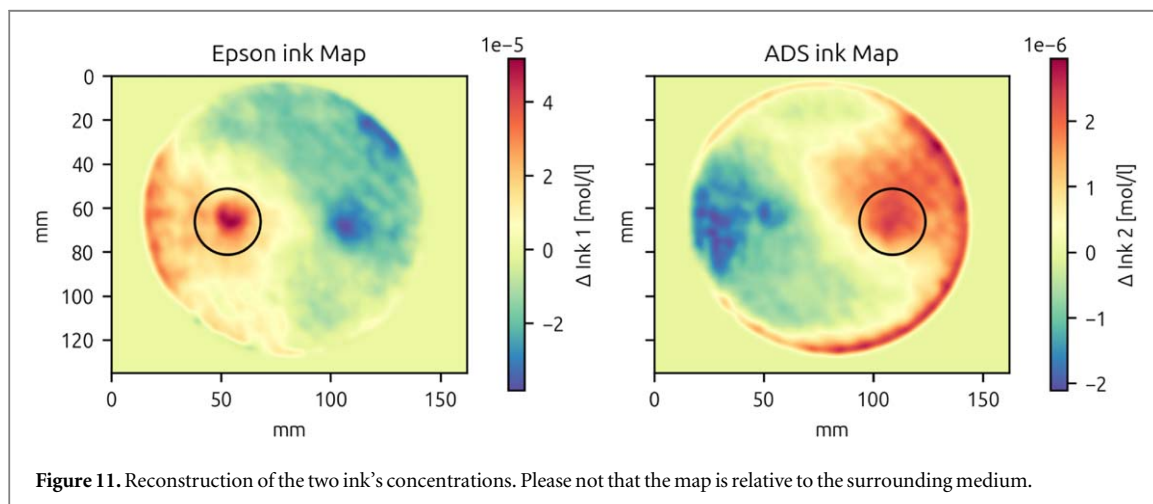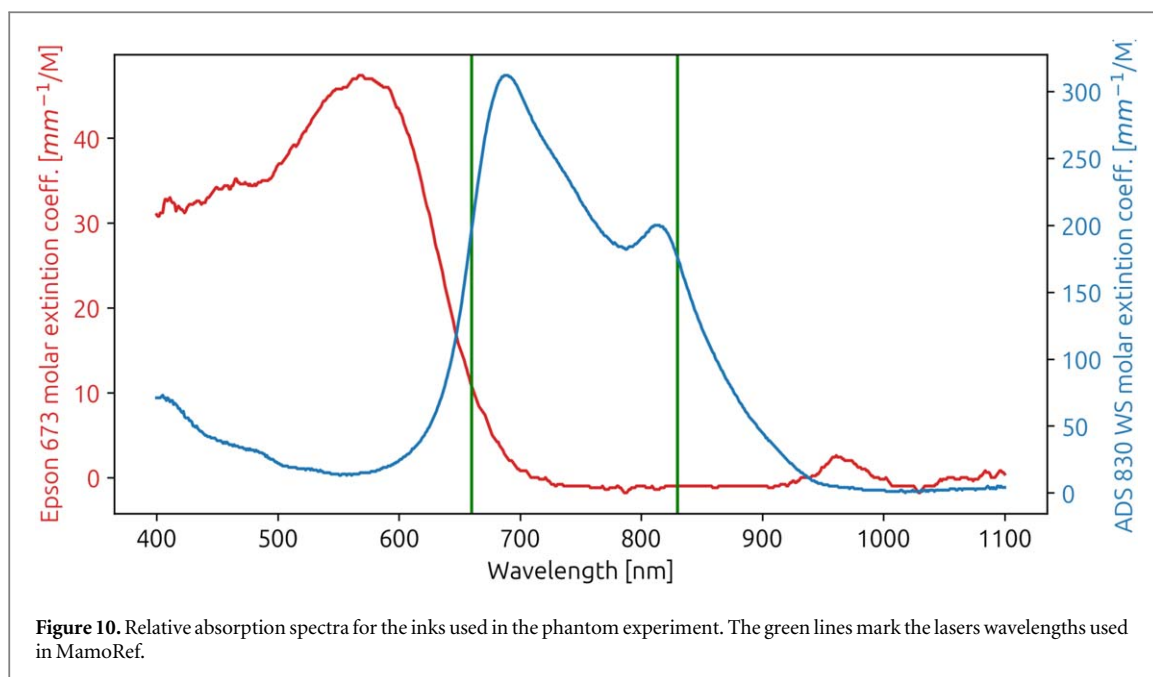
A phantom was constructed to include inclusions with varying relative absorption properties at the laser wavelengths employed by the device (660 and 830 nm). While our intention is not to precisely replicate the behavior of HbO and HbR, our objective in this study is to evaluate both the hardware and software components of MamoRef. To accomplish this, we employed two inks with distinct absorption spectra in the inclusions and attempted to determine the relative concentration of the inks using the input spectra data.

The homogeneous tissue was represented by a liquid phantom composed of a mixture of whole milk (Ilolay, 3% fat) and distilled water without any additional dye. The inclusions, which are solid, were created using a similar mixture of whole milk and distilled water, with the addition of agarose as a gelling agent (Laufer *et al* 2010). These inclusions were suspended at desired positions within the liquid medium using a stretched thread. Figure 9(a) depicts the inclusions as observed by MamoRef before the surrounding liquid medium was added.

To simulate the additional absorption of the inclusions, two types of inks were introduced. One inclusion was infused with ADS830WS dye obtained from American Dye Source (Ads830ws dye 2023). A $2 \times 10^{-6}\,\mathrm{g\,l^{-1}}$ solution of dye in distilled water was added to the preparation of the inclusion, resulting in an approximate dye concentration of $5.9 \times 10^{-7}\,\mathrm{mol\,l^{-1}}$. The other inclusion was supplemented with inkjet printer ink from Epson (model 673). Similarly to the previous case, a $3 \times 10^{-8}\,\mathrm{g\,l^{-1}}$ solution of ink was added to the preparation of the inclusion, resulting in an approximate ink concentration of $1.7 \times 10^{-6}\,\mathrm{mol\,l^{-1}}$. The absorption spectra of these inclusions are illustrated in figure 10.

In our experimental setup, we utilized the inks' spectra as a substitute for the HbO and HbR spectra commonly employed in clinical scenarios, to feed into our reconstruction algorithm. As in the case of MC simulations, the code can be seen in the GitHub repository (Github public repository of sample code 2023). Although this approach may not be entirely quantitative, it affords us the opportunity to examine the efficacy of the retrieval of relative concentration of chromophores, without the inherent challenges associated with using real oxygenated or deoxygenated blood samples. Notably, the use of blood samples in such analyzes can be logistically complex, time-consuming, and expensive, requiring specialized handling and storage facilities, as well as strict adherence to safety protocols.

The phantom was then measured in MamoRef as if it were a real breast. Figure 11 shows the result using the reconstruction applying the algorithms described in the previous section. It can be seem that the difference in absorption of both inclusions is clearly visible, and they are represented as difference in ink concentrations relative to the medium.

Figure 10. Relative absorption spectra for the inks used in the phantom experiment. The green lines mark the lasers wavelengths used in MamoRef.

Figure 11. Reconstruction of the two ink's concentrations. Please not that the map is relative to the surrounding medium.

It is crucial to consider that the concentration calculation of one ink should not be influenced by the presence of the absorber in the other inclusion. However, the inclusion filled with, for instance, Epson ink dilutes the other components, particularly the milk. As a result, there is a reduction in overall absorption at the opposite wavelength, leading to a negative concentration value in the region occupied by the Epson ink-filled inclusion when compared to the surrounding medium in the ADS ink map. The same effect is observed in reverse when analyzing the inclusion filled with ADS ink. This effect is compounded with the fact that the inclusions are made of agarose, which reduces its scattering coefficient. This reduction in scattering can be seen as an apparent reduction in absorption when measuring in CW regime.

While the recovered absolute values of the dye concentrations differ from the actual values, this disparity is consistent with findings in other studies that have utilized NIR techniques (Mozumder *et al* 2022). Furthermore, our primary objective is to create an accurate map of the relative concentrations of chromophores, and we have successfully captured the ratios between the inks.

3.3. Clinical research, feasibility study
As part of the on-going development work of MamoRef we conduce a clinical research with several objectives:

- Evaluate the feasibility of clinical use of MamoRef in patients with BIRADS (Radiology *et al* 2013) III–V breast nodules.

- Describe the findings of MamoRef images in patients with BIRADS III–V.

Figure 12. Voluntary team member laying on the stretcher to test the comfort of the assembly of MamoRef. Face and GUI image blurred for privacy.

- Characterize the clinical, imaging (x-ray mammography, breast ultrasound, and/or breast MRI), and histopathological profile of patients with BIRADS III–V.

- Identify patterns of NIR images obtained through MamoRef with their clinical-radiological and pathological counterparts.

These clinical trials are being done in conjunction with clinical researchers of the Hospital Privado de la Comunidad (HPC) (Hospital privado de la comunidad 2023) at their facilities. The HPC is a high-complexity hospital which since 2018 has had an accredited mastology unit by the Sociedad Argentina de Mastología (Argentine Society of Mastology). The hospital performs 460 breast surgeries per year and has a cohort of patients who are treated only in this hospital for all clinical, laboratory and imaging services, allowing for complete and long-term follow-up.
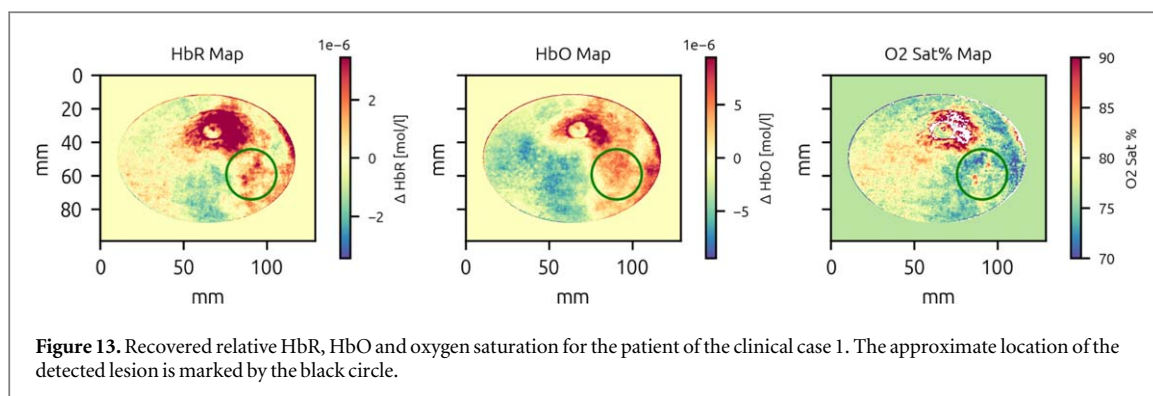
In this study, a detailed analysis was conducted on women diagnosed with BIRADS III, IV, V breast lesions. Patients who require biopsy or follow-up based on mammography or ultrasound findings, as recommended by their treating physician, were included. The inclusion criteria consisted of patients aged 18 years or older, who agreed to the informed consent process, had the ability to undergo the study, and whose results of the biopsy or further studies were available. Exclusion criteria included acute inflammatory lesions or conditions that could affect the near-infrared (NIR) signal, refusal to participate in informed consent, and inability to undergo the study due to physical-related issues. These criteria ensure the appropriate selection of patients for the study. All patients expressed written voluntary approval to be subjects of this study.

As mentioned above, the aim was to investigate and compare the characteristics and diagnostic outcomes of both benign and malignant lesions using various imaging techniques, including mammography and ultrasound, in conjunction with pathological anatomy findings. At the time of writing, 42 measurements have been made on voluntary subjects.

For the present contribution, we show two selected cases of the on-going feasibility study. They were chosen as representative cases and consist in one patient (clinical case 1) with (post-study) diagnosis of invasive ductal carcinoma; and one patient (clinical case 2) in which no malignant lesions were diagnosed.

3.3.1. Ergonomic and subjective feedback

One of the critical feedbacks to be obtained in the clinical viability trials is the subjective analysis given by the patients about the comfort and ergonomics of MamoRef. Figure 12 shows an anonymized photo of a voluntary patient being measured. It was reported that, while MamoRef is designed to be comfortable, the prone position in which the patient is placed can be uncomfortable after some time. In such respect, the first patients of the feasibility study reported that the device is comfortable enough for measurements of less than 10 min. With this information, we optimized the measurement parameters (number of scan positions, number of photos per positions) to ensure that no matter the case, the measurement will last no more than 10 min. As previously

Figure 13. Recovered relative HbR, HbO and oxygen saturation for the patient of the clinical case 1. The approximate location of the detected lesion is marked by the black circle.

mentioned, the mean number of scan positions in the 42 clinical cases up to the current date is 68. Multiplying this value by three lasers, and with a capture time of approximately 2 s, results in a mean scan time of just under 7 min.

3.3.2. Clinical case 1: malignant lesion
Description of mammography findings. The mammography examination reveals an ACR (Acr statement on reporting breast density in mammography reports and patient summaries 2023) type B pattern, indicating the presence of scattered and symmetrical fibroglandular tissue in the breast. In the upper outer quadrant of the left breast, specifically at hour 1, an oval-shaped lesion is observed. This lesion appears hyperdense with spiculated edges, and exhibits microcalcifications within it. The dimensions of the lesion are approximately 24 mm × 28 mm in diameter. Moreover, the lesion is causing retraction of the adjacent superficial planes. No significant abnormalities are detected in the right breast, and the axillary regions appear normal without any notable findings.

Description of ultrasound findings. The ultrasound examination reveals bilateral breast parenchyma characterized by a uniform and homogeneous fibroglandular echostructure. In the left breast, precisely at the hour 3 position, consistent with the clinical and mammographic findings, a nodular and bilobed image is observed. This image exhibits a partial echogenic halo and appears hypoechoic. Furthermore, the nodular lesion displays punctiform calcifications and shows the presence of vessels within it. The dimensions of the lesion are measured to be 18.6 × 9.7 mm. No abnormalities are detected in the axillary regions.

Considering both the mammography and ultrasound findings, the patient is categorized as BIRADS IV, indicating a suspicious lesion that requires further evaluation.

Pathological Anatomy Results. The macroscopic examination reveals the presence of six yellowish-white cylinders, with the largest measuring 1.5 cm in length. The diagnosis of the core biopsy taken from the left breast, specifically at the 3 o'clock position, indicates the presence of non-special type invasive carcinoma, specifically invasive ductal carcinoma. The histological assessment classifies the carcinoma as grade 2, with a nuclear grade of 3 and mitotic grade of 2, resulting in an overall Nottingham II grade.

The histological examination further identifies areas of necrosis, prominent fibrosis, and minimal peritumoral inflammatory reaction (TILs). Notably, there is no evidence of vascular invasion observed in the examined tissue.

Description of MamoRef findings. Figure 13 shows the results of MamoRef for the clinical case 1. The evaluation of the left breast reveals that the periphery of the upper and lower outer quadrants cannot be adequately assessed due to artifacts resulting from improper contact between the breast and the device window. However, in the central region, there is an area exhibiting enhanced metabolism, absorption, or uptake, which corresponds to the hyperpigmentation of the nipple.

At the periareolar level, a distinct region with increased metabolism, absorption, or uptake is observed. This region displays irregular margins and measures approximately 32 mm × 25 mm ± 0.5 mm. The characteristics of this area are indicative of a neoproliferative lesion, aligning with the findings obtained from both the mammography and ultrasound examinations.

3.3.3. Clinical Case 2: benign lesion
Description of ultrasound findings. The ultrasound examination reveals bilateral breast parenchyma characterized by a uniform and homogeneous fibroglandular echostructure.

In the left breast, specifically at the 7 o'clock position, an ovoid hypoechoic image is observed. This image exhibits well-defined and circumscribed margins, without apparent vascularization. The dimensions of the hypoechoic lesion are measured to be 23.3 mm. No abnormalities are detected in the axillary regions.

Figure 14. Recovered relative HbR, HbO and oxygen saturation for the patient of the clinical case 2.
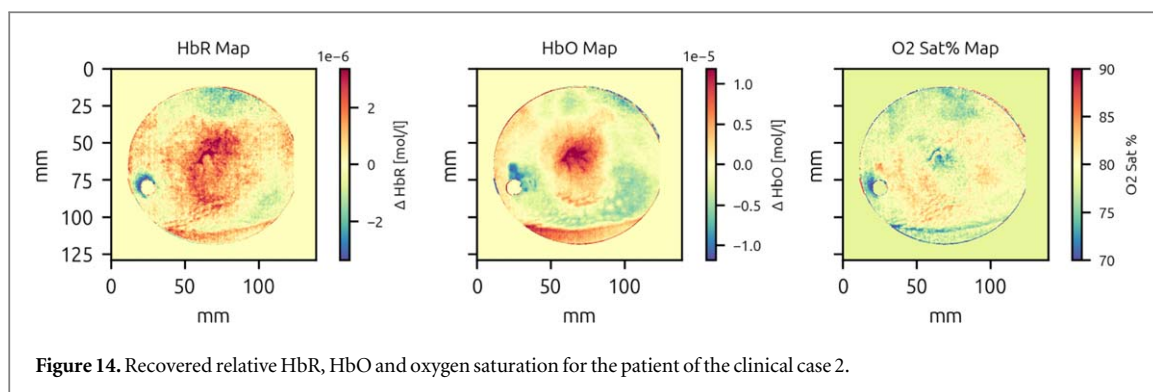
Considering these imaging findings, the patient is classified as BIRADS III, indicating a lesion with intermediate suspicion that requires short-term follow-up and further evaluation.

Pathological Anatomy Results. In the macroscopic examination, irregular cylinders of various sizes were received, with the largest measuring 0.6 cm. The diagnostic analysis focused on the left breast, specifically at clock position 7, using a core biopsy technique. The findings obtained were indicative of a fibroadenoma, a common benign breast tumor. Notably, no signs of atypia or abnormal cell growth were observed during the examination.

Description of MamoRef findings. Figure 14 shows the results of MamoRef for the clinical case 2. Similar to the previous case, the region of increased metabolism or absorption in the breast corresponds to the hyperpigmentation of the nipple.

No focal areas with increased metabolism or absorption are identified in the current study, indicating the absence of metabolically active lesions. It is important to note that fibroadenomas, which are known to have limited vascularity and metabolic activity, are consistent with these findings.

The circular artifact present in the bottom-left quadrant of the maps is a result of an undesired reflection affecting the CCD sensor. It was removed during post-processing, which resulted in an area with missing information. This issue has been resolved in subsequent measurements through hardware adjustments.

4. Conclusions

In this study, we have presented a comprehensive investigation of the MamoRef device, a Near-infrared Spectroscopy (NIRS) device designed for the assessment of breast lesions. We have successfully demonstrated its practical implementation and its potential as a diagnostic tool for breast cancer detection.

The study began by introducing the theoretical background and working principle of the MamoRef device, followed by a detailed description of the technical specifications of its hardware and software components. Through Monte Carlo simulations, we validated the accuracy of the reconstruction algorithm, confirming the effectiveness of the device. Phantom tests were conducted to assess the capability of MamoRef in detecting inclusions representing different types of breast lesions.

Building on these results, we collaborated with clinical researchers, physicians, and medical technicians to design a clinical feasibility study. The objective of this study is to evaluate the feasibility of MamoRef as a diagnostic device by identifying patterns in NIR images obtained through the device that can differentiate various types of breast lesions. While the study is still ongoing, the initial results are highly encouraging and demonstrate the potential of MamoRef as an effective diagnostic tool for breast cancer detection.

Based on the positive outcomes observed thus far, we plan to move forward with seeking regulatory approval for MamoRef, should these outcomes persist throughout the duration of the trial. To support subsequent clinical trials and regulatory submissions, our goal is to develop a next-generation MamoRef prototype optimized for pivotal clinical trials and larger-scale manufacturing. This new iteration will need to be more robust, dependable, and reproducible than the current version.

While the reconstruction algorithm presented in this study has proven to be functional and sufficiently informative for drawing preliminary conclusions regarding the feasibility of our approach, there exist several areas where significant enhancements are both feasible and beneficial. One limitation is the absence of 3D information in our current reconstruction. To address this, we propose an extension of our NIR tomosynthesis methodology (Carbone *et al* 2021) to incorporate reflectance geometries, enabling the derivation of valuable 3D data.

Another challenge we encountered pertains to the region surrounding and situated behind the nipple. In our current implementation, we have introduced a reference image capture step to assist users and medical

personnel in identifying the nipple's position and, when feasible, avoiding occlusion of the region of interest. However, this issue remains an ongoing concern, prompting the need for further research and algorithmic refinement. Future work will explore the development of algorithms capable of generating robust 3D information, potentially offering improved solutions to address this specific challenge.

In addition, we are exploring the integration of Artificial Intelligence (AI) algorithms to enhance the performance of the proposed reconstruction algorithm in this study. Although limited training data poses a challenge, supplementing Monte Carlo simulations with instrument calibration data may suffice for conducting a preliminary proof-of-concept. Furthermore, MamoRef can serve as an additional source of information, augmenting the capabilities of AI algorithms to effectively distinguish between various types of breast lesions.

This research contributes to the growing body of literature on NIRS devices and their application in breast cancer diagnosis. The success of the MamoRef device in detecting different types of breast lesions, along with its promising results in ongoing clinical trials, holds significant potential for improving breast cancer diagnosis and treatment. With further development and refinement, MamoRef has the capability to make a substantial impact on breast cancer management, ultimately leading to improved patient outcomes. This potential is enhanced by the relative simplicity and low cost of the device, with a current bill of materials (in a prototype stage) of under $20.000 and a design that emphasizes portability and robustness.

Acknowledgments

This contribution presents the results of a research study involving human participants. The study adhered to the principles outlined in the Declaration of Helsinki and complied with local statutory requirements. All patients provided informed written consent, and all results were anonymized following standard industry practices. The research protocol received approval from the ethics committee of the Hospital Privado de la Comunidad and was also approved by the Ministerio de Salud de la Provincia de Buenos Aires under ID nro. 2919-2744/2022.

The authors have confirmed that any identifiable participants in this study have given their consent for publication.

Data availability statement

The data that support the findings of this study are openly available at the following URL/DOI: https://github.com/nicocarbone/MamoRefCodePublic.

ORCID iDs

Nicolás A Carbone ⓘ https://orcid.org/0000-0002-5452-1165
Demián A Vera ⓘ https://orcid.org/0000-0002-6788-888X
M Victoria Waks-Serra ⓘ https://orcid.org/0000-0002-9888-7740
Héctor A García ⓘ https://orcid.org/0000-0002-5142-7149

References

Acr statement on reporting breast density in mammography reports and patient summaries http://acr.org/Advocacy-and-Economics/ACR-Position-Statements/Reporting-Breast-Density. Accessed: 2023-05-16.
Ads830ws dye 2023 https://adsdyes.com/products/nir_dyes/ads830ws/ Accessed: 2023-04-27
Almajidy R K, Mankodiya K, Abtahi M and Hofmann U G 2020 A newcomer's guide to functional near infrared spectroscopy experiments *IEEE Rev. Biomed. Eng.* **13** 292–308
Belia F *et al* 2022 The use of indocyanine green (ICG) and near-infrared (NIR) fluorescence-guided imaging in gastric cancer surgery: a narrative review *Front. Surg.* **9** 880773
Berg W A, Bandos A I, Mendelson E B, Lehrer D, Jong R A and Pisano E D 2016 Ultrasound as the primary screening test for breast cancer: analysis from acrin 6666, JNCI *J. Natl Cancer Institute* **108** djv367
Biswal N C, Xu Y and Zhu Q 2011 Imaging tumor oxyhemoglobin and deoxyhemoglobin concentrations with ultrasound-guided diffuse optical tomography *Technol. Cancer Res. Treat.* **10** 417–29
Brunet D, Vrscay E R and Wang Z 2011 On the mathematical properties of the structural similarity index *IEEE Trans. Image Process.* **21** 1488–99
Busch D R, Choe R, Durduran T and Yodh A G 2013 Toward noninvasive characterization of breast cancer and cancer metabolism with diffuse optics *PET Clin.* **8** 345–65

Carbone N, Iriarte D, Pomarico J, Grosenick D and Macdonald R 2015 Cw fluorescence imaging of tissue-like media in reflectance geometry *European Conference on Biomedical Optics* (Optica Publishing Group) 95381E

Carbone N, Iriarte D and Pomarico J 2017 Wide field continuous wave reflectance optical topography including a clear layer on top of the diffusive surface *J. Near Infrared Spectrosc.* **25** 165–71

Carbone N A, Baez G R, García H A, Serra M V W, Rocco H O D, Iriarte D I, Pomarico J A, Grosenick D and Macdonald R 2014 Diffuse reflectance optical topography: location of inclusions in 3d and detectability limits *Biomed. Opt. Express* **5** 1336–54

Carbone N A, Pomarico J A and Iriarte D I 2017 Gpu accelerated monte carlo simulation of light propagation in inhomogeneous fluorescent turbid media. Application to whole field CW imaging *Biomed. Phys. Eng. Express* **3** 4045012

Carbone N A 2017 *Tesis de Doctorado: Estudio de la formación de imágenes en geometrías de reflectancia usando luz de onda continua en el infrarrojo cercano—Aplicación a la mamografía* Universidad Nacional del Centro de la Provincia de Buenos Aires

Carbone N A, Vera D A, Iriarte D I, Pomarico J A, Macdonald R and Grosenick D 2021 Reconstruction of absorption maps by digital tomosynthesis *European Conference on Biomedical Optics* (Optica Publishing Group) pp EM3C–5

Chiarelli A M, Blackmore K M, Mirea L, Done S J, Majpruz V, Weerasinghe A, Rabeneck L and Muradali D 2020 Annual vs biennial screening: diagnostic accuracy among concurrent cohorts within the ontario breast screening program *JNCI: J. Natl Cancer Institute* **112** 400–9

Coherent stingray diode lasers https://coherent.com/lasers/diode-modules/stingray-bioray Accessed: 2023-04-13

Contini D, Martelli F and Zaccanti G 1997 Photon migration through a turbid slab described by a model based on diffusion approximation: I. Theory *Appl. Opt.* **36** 4587–99

Dosselmann R and Yang X D 2011 A comprehensive assessment of the structural similarity index *Signal Image and Video Processing* (Germany: Springer) vol 5, pp 81–91

Ferlay J, Colombet M, Soerjomataram I, Parkin D M, Piñeros M, Znaor A and Bray F 2021 Cancer statistics for the year 2020: an overview *Int. J. Cancer* **149** 778–89

Github public repository of sample code https://github.com/nicocarbone/MamoRefCodePublic Accessed: 2023-04-27

Groen E J, Elshof L E, Visser L L, Emiel J, Winter-Warnars H A, Lips E H and Wesseling J 2017 Finding the balance between over-and under-treatment of ductal carcinoma *in situ* (DCIS) *Breast* **31** 274–83

Hachey K J, Digesu C S, Armstrong K W, Gilmore D M, Khullar O V, Whang B, Tsukada H and Colson Y L 2017 A novel technique for tumor localization and targeted lymphatic mapping in early-stage lung cancer *J. Thoracic Cardiovasc. Surg.* **154** 1110–8

Herranz M *et al* 2012 Optical imaging in breast cancer diagnosis: the next evolution *J. Oncol.* **2012** 10863747

Hiraoka M, Firbank M, Essenpreis M, Cope M, Arridge S, van der Zee P and Delpy D 1993 A monte carlo investigation of optical pathlength in inhomogeneous tissue and its application to near-infrared spectroscopy *Phys. Med. Biol.* 1859–76

Homer M J 1985 Breast imaging: pitfalls, controversies, and some practical thoughts *Radiol. Clin. North Am.* **23** 459–72

Hoogstins C E *et al* 2018 Image-guided surgery in patients with pancreatic cancer: first results of a clinical trial using sgm-101, a novel carcinoembryonic antigen-targeting, near-infrared fluorescent agent *Ann. Surg. Oncol.* **25** 3350–7

Hospital privado de la comunidad https://hpc.org.ar/ Accessed: 2023-04-20

Huda W and Abrahams R B 2015 X-ray-based medical imaging and resolution *Am. J. Roentgenol.* **204** W393–7

Jacques S L 2013 Optical properties of biological tissues: a review *Phys. Med. Biol.* **58** R37

Kim M N *et al* 2010 Noninvasive measurement of cerebral blood flow and blood oxygenation using near-infrared and diffuse correlation spectroscopies in critically brain-injured adults *Neurocrit. Care* **12** 173–80

Kocsis L, Herman P and Eke A 2006 The modified Beer–Lambert law revisited *Phys. Med. Biol.* **51** N91–8

Kondepati V R, Zimmermann J, Keese M, Sturm J, Manegold B C and Backhaus J 2005 Near-infrared fiber optic spectroscopy as a novel diagnostic tool for the detection of pancreatic cancer *J. Biomed. Opt.* **10** 054016

Laufer J, Zhang E and Beard P 2010 Evaluation of absorbing chromophores used in tissue phantoms for quantitative photoacoustic spectroscopy and imaging *IEEE J. Sel. Top. Quantum Electron.* **16** 600–7

Lin E and Alessio A 2009 What are the basic concepts of temporal, contrast, and spatial resolution in cardiac CT? *J. Cardiovasc. Comput. Tomogr.* **3** 403–8

Lu J *et al* 2009 Breast cancer metastasis: challenges and opportunities *Cancer Res.* **69** 4951–3

Luo C, Li N, Lu B, Cai J, Lu M, Zhang Y, Chen H and Dai M 2022 Global and regional trends in incidence and mortality of female breast cancer and associated factors at national level in 2000 to 2019 *Chin. Med. J.* **135** 42–51

Martelli F, Binzoni T, Del Bianco S, Liemert A and Kienle A 2022 *Light Propagation through Biological Tissue and Other Diffusive Media* (United States: SPIE) 2nd edn (https://doi.org/10.1117/3.824746)

Maziak D E, Do M T, Shamji F M, Sundaresan S R, Perkins D G and Wong P T 2007 Fourier-transform infrared spectroscopic study of characteristic molecular structure in cancer cells of esophagus: an exploratory study *Cancer Detect. Prevention* **31** 244–53

Monte Carlo extreme https://mcx.space/ Accessed: 2023-04-20

Mozumder M, Leskinen J and Tarvainen T 2022 Utilising nanosecond sources in diffuse optical tomography *Meas. Sci. Technol.* **34** 025901

Nioka S and Chance B 2005 Nir spectroscopic detection of breast cancer *Technol. Cancer Res. Treat.* **4** 497–512

Ntziachristos V and Chance B 2000 Breast imaging technology: probing physiology and molecular function using optical imaging-applications to breast cancer *Breast Cancer Res.* **3** 1–6

Parikh U, Chhor C M and Mercado C L 2018 Ductal carcinoma *in situ*: the whole truth *Am. J. Roentgenol.* **210** 246–55

Pdq15-q48-s15-d power supply 2023 https://digikey.com/en/products/detail/cui-inc/PDQ15-Q48-S15-D/6165398. Accessed: 2023-04-18

Pellicer A and Bravo M C 2011 Near-infrared spectroscopy: a methodology-focused review *Semin. Fetal Neonatal Med.* **16** 42–9

Portnow L H, D'Alessio D, Morris E A, Bernard-Davila B and Mango V L 2021 Palpable breast findings in high-risk patients: are self-and clinical breast exams worthwhile? *J. Breast Imaging* **3** 190–5

Prince S and Malarvizhi S 2007 Monte Carlo simulation of nir diffuse reflectance in the normal and diseased human breast tissues *BioFactors* **30** 255–63

Radiology A C *et al* 2013 A.C. Radiology et al, ACR BI-RADS atlas: breast imaging and reporting and data system; mammography, ultrasound, magnetic resonance imaging, follow-up and outcome monitoring, data dictionary. ACR, American College of Radiology

Rinneberg H, Grosenick D, Moesta K T, Mucke J, Gebauer B, Stroszczynski C, Wabnitz H, Moeller M, Wassermann B and Schlag P M 2005 Scanning time-domain optical mammography: detection and characterization of breast tumors in vivo *Technol. Cancer Res. Treat.* **4** 483–96

Serra M W, Grau V N, Vera D, Jodra S, García H, Carbone N, Pardini P, Pomarico J and Iriarte D 2022 Anthropomorphic polydimethylsiloxane silicone-based phantom for diffuse optical imaging *Heliyon* **8** e10308

Shi Z and Anderson C A 2010 Application of monte carlo simulation-based photon migration for enhanced understanding of near-infrared (nir) diffuse reflectance: I. Depth of penetration in pharmaceutical materials *J. Pharm. Sci.* **99** 2399–412

Stm32f103 microcontroller 2023 https://st.com/en/microcontrollers-microprocessors/stm32f103.html Accessed: 2023-04-26

Sun X, Xu Y, Wu J, Zhang Y and Sun K 2013 Detection of lung cancer tissue by attenuated total reflection-fourier transform infrared spectroscopy—a pilot study of 60 samples *J. Surg. Res.* **179** 33–8

Sung H, Ferlay J, Siegel R L, Laversanne M, Soerjomataram I, Jemal A and Bray F 2021 Global cancer statistics 2020: globocan estimates of incidence and mortality worldwide for 36 cancers in 185 countries *CA: Cancer J. Clin.* **71** 209–49

Suzaki H, Kobayashi N, Nagaoka T, Iwasaki K, Umezu M, Takeda S and Togawa T 2006 *28th Annual Int. Conf. of the IEEE Engineering in Medicine and Biology Society, EMBS'06 Noninvasive measurement of total hemoglobin and hemoglobin derivatives using multiwavelength pulse spectrophotometry -in vitro study with a mock circulatory system* (*Annual Int. Conf. of the IEEE Engineering in Medicine and Biology—Proc.*) pp 799–802

Tabar L *et al* 2018 Effect of mammography screening on mortality by histological grade, Cancer Epidemiology *Biomarkers Prevention* **27** 154–7

Tabulated molar extinction coefficient for hemoglobin in water https://omlc.org/spectra/hemoglobin/summary.html Accessed: 2022-10-09

Taroni P, Paganoni A M, Ieva F, Pifferi A, Quarto G, Abbate F, Cassano E and Cubeddu R 2017 Non-invasive optical estimate of tissue composition to differentiate malignant from benign breast lesions: a pilot study *Sci. Rep.* **7** 40683

Teh S K, Zheng W, Ho K Y, Teh M, Yeoh K G and Huang Z 2008 Diagnosis of gastric cancer using near-infrared raman spectroscopy and classification and regression tree techniques *J. Biomed. Opt.* **13** 034013

Thorlabs cs505mu 2023 web page. https://thorlabs.com/ thorproduct.cfm?partnumber=CS505MU Accessed: 2023-04-13

Thorlabs gvs012/m2023—2d large beam (10 mm) diameter galvo system. https://www.thorlabs.com/ thorproduct.cfm?partnumber=GVS012/M. Accessed: 2023-04-13

Thorlabs mvl12m1 2023 web page https://thorlabs.com/thorproduct.cfm?partnumber=MVL12M1 Accessed: 2023-04-13

Tromberg B J, Shah N, Lanning R, Cerussi A, Espinoza J, Pham T, Svaasand L and Butler J 2000 Non-invasive in vivo characterization of breast tumors using photon migration spectroscopy *Neoplasia* **2** 26–40

Tromberg B J *et al* 2016 Predicting responses to neoadjuvant chemotherapy in breast cancer: Acrin 6691 trial of diffuse optical spectroscopic imagingoptical imaging of breast cancer chemotherapy response *Cancer Res.* **76** 5933–44

Van Luijt P, Heijnsdijk E, Fracheboud J, Overbeek L, Broeders M, Wesseling J, den Heeten G and de Koning H 2016 The distribution of ductal carcinoma *in situ* (DCIS) grade in 4232 women and its impact on overdiagnosis in breast cancer screening *Breast Cancer Res.* **18** 1–10

Vasudevan S, Campbell C, Liu F and O'Sullivan T D 2021 Broadband diffuse optical spectroscopy of absolute methemoglobin concentration can distinguish benign and malignant breast lesions *J. Biomed. Opt.* **26** 065004

Vera D A, García H A, Serra M V W, Baez G R, Iriarte D I and Pomarico J A 2022 A monte carlo study of near infrared light propagation in the human head with lesionsa time-resolved approach *Biomed. Phys. Eng. Express* **8** 035005

Vo-Dinh T 2002 *Biomedical Photonics Handbook* (Boca Raton: CRC Press) (https://doi.org/10.1201/b17289)

Weinstein S P, Localio A R, Conant E F, Rosen M, Thomas K M and Schnall M D 2009 Multimodality screening of high-risk women: a prospective cohort study *J. Clin. Oncol.* **27** 6124

Yen M-F, Tabar L, Vitak B, Smith R, Chen H-H and Duffy S 2003 Quantifying the potential problem of overdiagnosis of ductal carcinoma *in situ* in breast cancer screening *Eur. J. Cancer* **39** 1746–54

Zhang J, Zhang Z, Xiang Y, Dai Y and Harrington P D B 2011 An emphatic orthogonal signal correction-support vector machine method for the classification of tissue sections of endometrial carcinoma by near infrared spectroscopy *Talanta* **83** 1401–9

Zhang M, Li S, Zou Y and Zhu Q 2021 Deep learning-based method to accurately estimate breast tissue optical properties in the presence of the chest wall *J. Biomed. Opt.* **26** 106004

Zhao Y, Burger W R, Zhou M, Bernhardt E B, Kaufman P A, Patel R R, Angeles C V, Pogue B W, Paulsen K D and Jiang S 2017 Collagen quantification in breast tissue using a 12-wavelength near infrared spectral tomography (NIRST) system *Biomed. Opt. Express* **8** 4217–29

16-bit single channel 2023 serial interface, +/-18 V (high voltage bipolar) output dac https://www.ti.com/product/DAC8871 Accessed: 2023-04-18